MICROSCOPY

Nanoscale chemical imaging by photoinduced force microscopy

10.1126/sciadv.1501571

Derek Nowak,[1] William Morrison,[1] H. Kumar Wickramasinghe,[2] Junghoon Jahng,[3] Eric Potma,[4] Lei Wan,[5] Ricardo Ruiz,[5] Thomas R. Albrecht,[5] Kristin Schmidt,[6] Jane Frommer,[6] Daniel P. Sanders,[6] Sung Park[1]*

Correlating spatial chemical information with the morphology of closely packed nanostructures remains a challenge for the scientific community. For example, supramolecular self-assembly, which provides a powerful and low-cost way to create nanoscale patterns and engineered nanostructures, is not easily interrogated in real space via existing nondestructive techniques based on optics or electrons. A novel scanning probe technique called infrared photoinduced force microscopy (IR PiFM) directly measures the photoinduced polarizability of the sample in the near field by detecting the time-integrated force between the tip and the sample. By imaging at multiple IR wavelengths corresponding to absorption peaks of different chemical species, PiFM has demonstrated the ability to spatially map nm-scale patterns of the individual chemical components of two different types of self-assembled block copolymer films. With chemical-specific nanometer-scale imaging, PiFM provides a powerful new analytical method for deepening our understanding of nanomaterials.

INTRODUCTION

Ambient nondestructive topographic and chemical measurements of nanoscale materials and supramolecular structures are essential in research, development, and manufacturing in a variety of fields, including microelectronics, composite materials, nanotechnology, and life sciences. For example, supramolecular self-assembly of block copolymer (BCP) films is a promising method to extend nanofabrication beyond the limits of optical lithography, readily producing periodic structures with periods of 10 to 100 nm (*1*); to advance this class of materials, there is a pressing need for an analytical technique with a high degree of chemical specificity and spatial resolution. Direct spatiochemical imaging of the specific domains and defect structures in self-assembled BCP patterns will provide valuable information about the materials, process, and pattern quality (*2*). Current investigations in real space are based on electron microscopy (EM) techniques, atomic force microscopy (AFM), and near-field optics, all with limitations.

Recent EM-based spectroscopic advancements with energy-filtered transmission EM (*3*) can provide limited information for the identification of BCPs by inference with atomic *Z* contrast. For typical EM studies, selective staining (*4*), etching, or infiltration (*5*, *6*) of another compound inside one of the polymer constituents is used to further enhance the imaging contrast. However, such infiltration, staining techniques, or partial etching may alter or distort domain shape and/or boundary profiles (*7*). Even in systems where sufficient imaging contrast is available, electron beam damage caused during imaging may adversely affect the sample's characterization.

Optical spectroscopy provides the most promising noninvasive method to probe the chemical structure of BCPs. In particular, Fourier transform infrared (FTIR) spectroscopy provides noninvasive chemical-specific spectra for organic materials such as BCPs. The spatial resolution of traditional FTIR techniques is diffraction-limited, unable to resolve the fine BCP patterns. Recent advances in tip-enhanced scanning near-field optical imaging demonstrate the potential to extend spectroscopic imaging resolutions into the sub–10-nm range by combining optical spectroscopy with AFM (*8*–*10*). Examples of tip-enhanced near-field vibrational spectroscopy include tip-enhanced Raman scattering (TERS) (*11*–*13*) and infrared-scattering scanning near-field optical microscopy (IR s-SNOM) techniques (*14*–*16*). A general challenge for tip-enhanced measurements is the overwhelming background signal generated by the far-field scattered photons from the region surrounding the tip apex. With TERS, the lack of imaging probes that reliably enhance the near-field Raman scattering compared to the far-field scattering has held back its wide adoption, despite its promise (*17*). Furthermore, polymer blends and BCP systems do not lend themselves to resonant Raman enhancements, requiring long signal integration times (*18*). For IR s-SNOM, interferometry-based detection methods can provide effective background suppression (*10*, *15*). The IR s-SNOM images of relatively large self-assembled patterns (~80-nm pitch) of poly(styrene-*b*-methyl methacrylate) (PS-*b*-PMMA) BCP have demonstrated contrast between the two-block components by using the poly(methyl methacrylate) (PMMA) absorption band at 1733 cm^{-1} (*16*).

Another approach to achieve nanoscale absorption spectroscopy is to measure the thermal expansion of the sample caused by the photoabsorption locally via AFM. This technique, called photoexpansion (or photothermal) microscopy, uses contact-mode AFM to measure the expansion of the sample due to mid-IR laser absorption that is modulated at the cantilever's contact mechanical resonance (*19*). Although the typical spatial resolution of photothermal microscopy is on the order of 100 nm (*20*), a spatial resolution of about 20 nm was recently demonstrated by imaging a 2-nm-thick monolayer of self-assembled molecules on a gold surface, by taking advantage of the electromagnetic enhancement of the optical field intensity in the nanogap between a sharp gold-coated AFM tip and a gold-coated substrate (*21*). The resolution, sensitivity, and extendibility of this method may be limited by frictional forces that arise when operating in hard contact with the sample surface, particularly on soft samples; the low quality factor ($Q \sim 100$) that results from operating in hard contact (*22*); and the need for optical enhancement via specific substrate materials and ultrathin sample films to resolve features at the ~20-nm scale.

[1]Molecular Vista Inc., 6840 Via Del Oro, Suite 110, San Jose, CA 95119, USA. [2]Department of Electrical Engineering and Computer Science, University of California, Irvine, Irvine, CA 92697, USA. [3]Department of Physics and Astronomy, University of California, Irvine, Irvine, CA 92697, USA. [4]Department of Chemistry, University of California, Irvine, Irvine, CA 92697, USA. [5]HGST San Jose Research Center, 3403 Yerba Buena Road, San Jose, CA 95135, USA. [6]IBM Research–Almaden, 650 Harry Road, San Jose, CA 95120, USA.
*Corresponding author. E-mail: sung@molecularvista.com

Recognizing that the dipole-dipole interaction, which creates the near-field scattered photons in s-SNOM, should generate measurable attractive force, Rajapaksa *et al.* demonstrated mechanical detection of molecular resonance. The technique, now called photoinduced force microscopy (PiFM), can measure both linear (*23*) and nonlinear (*24*) sample polarizability by detecting the force gradient between the interaction of the optically driven molecular dipole and its mirror image dipole in a metal-coated AFM tip. This near-field excitation and near-field detection (as opposed to near-field excitation and far-field detection in other tip-enhanced near-field optical microscopy techniques described earlier) allow the detection of near-field optical response with no far-field background contribution (*23*–*26*). The use of dynamic AFM (also known as tapping mode or noncontact AFM) provides good sensitivity due to the high quality factor ($Q \sim 600$) of the cantilever and minimal tip-sample interaction, making it ideal for soft matter such as BCPs. Here, we present infrared PiFM (IR PiFM) results in the molecular fingerprint region of the spectrum, demonstrating high spatial resolution and a true chemical specificity by separately resolving and positively identifying each domain in self-assembled patterns of two different BCP systems with ~40-nm pitch.

Theory of photoinduced force

The photoinduced force is the result of a dipole-dipole force attraction between the imaging tip and the sample when illuminated with a monochromatic, coherent light source. Considering a system of two polarizable spheres, the time-averaged photoinduced force was described by Dholakia and Zemánek (*27*) and by Arias-González and Nieto-Vesperinas (*28*) as

$$\langle F \rangle \propto Re\left\{ \sum_i P_i^*(r)\, \nabla E_i(r) \right\} \quad (1)$$

where $i = x, y, z$; $P^*(r)$ describes the optically induced polarization of the tip; and $\nabla E(r)$ is the gradient of the optical electric field in the vicinity of the tip, influenced by the polarization of the sample. This polarization-induced force can be expressed as the sum of a localized force F_{loc}, which is dependent on the tip-sample distance, and a nonlocalized force F_{nloc}, which is independent of the tip-sample distance at the nanoscale (*27*, *29*). Summed together, the resultant time average force can be expressed as

$$\langle F \rangle = F_{loc} + F_{nloc} \quad (2)$$

Assuming that the spatial phase of the electric field remains unchanged in the tip-sample junction, the force expression for the localized and nonlocalized force can be expressed as (*30*)

$$F_{loc} \propto -\frac{1}{z^4} Re\{a_s a_t^*\} |E_z|^2 \quad (3)$$

$$F_{nloc} \propto Im\{a_t\} |E_x|^2 \quad (4)$$

where α_s and α_t are the polarizabilities of the sample and tip, respectively. Here, E_x and E_z are the x and z components of the incident field. The E_z dependence and the $1/z^4$ nature of the F_{loc} lead to the highly localized force behavior in PiFM, which is the basis of PiFM's high spatial resolution. By expressing the polarizability as $\alpha = \alpha' + i\alpha''$, where α' is a real part of polarizability and α'' is an imaginary part of polarizability, the localized force depends on $\alpha_s'\alpha_t' + \alpha_s''\alpha_t''$. On the other hand, the nonlocalized force lacks this spatial confinement. Therefore, under tip-sample distances of tens of nanometers, the localized force is the dominant contribution to the image contrast. In the measured experiment, the localized force contribution dominates at a tip-sample distance of less than ~30 nm (discussed in Results section). The magnitude of the resulting force depends on the balance between the real and imaginary polarizabilities of the sample and tip. Depending on the tip and sample resonances, the measured force is dominated by either the $\alpha_s'\alpha_t'$ or the $\alpha_s''\alpha_t''$ term. In the mid-IR excitation measurements that follow, we used gold tips that have a large imaginary (k) index, emphasizing the $\alpha_s''\alpha_t''$ term and providing a sensitive measurement of the imaginary part of the sample's polarizability.

RESULTS

Experimental setup

To demonstrate PiFM using mid-IR excitation, we probe the force generated by the molecular polarizability of BCPs. A commercial AFM microscope operated in dynamic noncontact mode with an integrated off-axis parabolic mirror is used (conceptually shown in Fig. 1). The excitation source is a tunable mid-IR quantum cascade laser (QCL) with a pulse width of 30 ns and an adjustable repetition rate that is set to the difference frequency between the first and second mechanical resonances of the AFM cantilever, approximately 1.6 MHz for this study. The AFM is operated so that the second mechanical mode detects the surface topography and the first mechanical mode detects the photoinduced force. The cantilever resonances are independent eigenmodes, allowing for the topography and PiFM to be recorded simultaneously without crosstalk. The excitation laser is focused by the parabolic mirror to an elliptical spot with a size of 2λ and 2.5λ for the short axis and long axis, respectively. An average laser power of 1.0 mW is used at the sample surface.

Isolating the photoinduced force

The localized nature of the force in the PiFM measurement in the mid-IR is confirmed by tip-sample distance curves taken on a 10-nm-thick poly(styrene-*r*-epoxydicyclopentadiene methacrylate) (PS-*r*-PEDCPMA) brush prepared on Si excited with 1733 cm^{-1}, a known resonance for PMMA, as shown in Fig. 2. We compare the effects of exciting the cantilever by direct-drive modulation, contact resonance, and sideband modulation (the mode used to obtain the experimental results on the BCPs). The principle of direct mode is to modulate the laser intensity at the cantilever detection frequency, in our case the first mechanical resonance ($f_m = f_0$), to probe all the photoinduced forces, both localized and nonlocalized (*25*). In Fig. 2, the green line is the result of the direct-drive modulation. Because the localized force is attractive whereas the nonlocalized force is repulsive, the curve should show a cancellation point where $F_{loc} + F_{nloc} = 0$, which appears at the minimum point in the green curve around 32 nm. An offset underneath the cancellation point is due to the thermal vibrational noise of the cantilever. This can be reduced by using a high stiffness cantilever with higher mechanical resonance frequency (*25*, *30*). As the tip gets closer to the sample surface, the PiFM amplitude increases due to the growing localized optical force until (around the 7-nm point in the green curve in Fig. 2) the mechanical force gradient from conservative forces such as van der Waals and dissipative forces start to decrease the amplitude (via the shifting of the detection resonance frequency). When the tip comes into hard contact with the surface (defined as zero AC amplitude), the free mechanical resonance

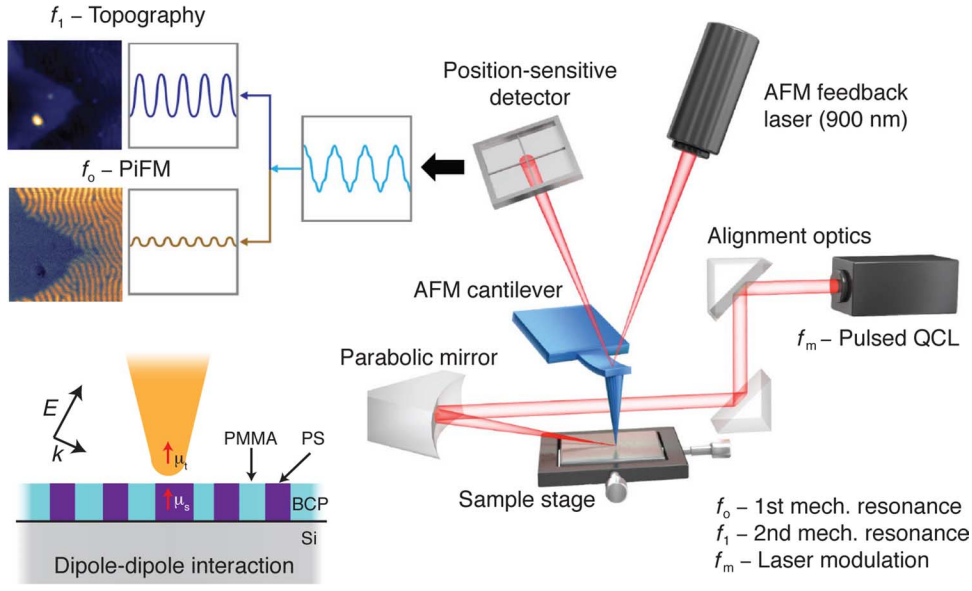

Fig. 1. Schematic of IR PiFM experiment. The incident mid-IR laser is electrically triggered to pulse at $f_m = f_1 - f_0$, where f_0 and f_1 are the first and second mechanical eigenmode resonances of the cantilever. The topography of the sample is recorded by the AFM feedback system at f_1, and the PiFM is concurrently recorded at f_0 by the feedback laser position-sensitive detector and lock-in electronics. The sample is raster-scanned under the tip to generate the image. The incident light is polarized along the tip axis to maximize the signal coupling of the dipole-dipole force along the vertical direction of the cantilever vibration.

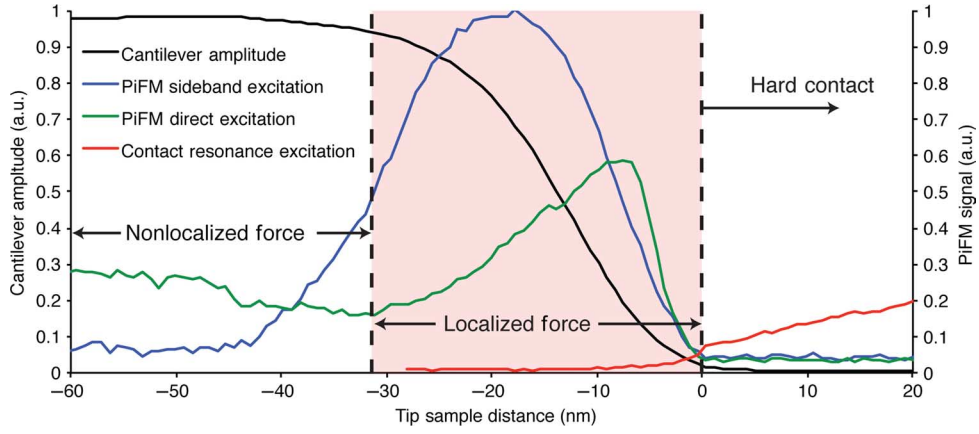

Fig. 2. The PiF signal and cantilever amplitude as a function of tip-sample distance on 10-nm-thick PS-*r*-PEDCPMA brush prepared on Si and excited with 1733 cm^{-1}. The black curve is the amplitude curve of the second resonance, which probes the topography in a dynamic AFM mode. The green curve is the amplitude of the first mechanical resonance, used for probing the photoinduced force with direct-drive modulation to measure both the localized and nonlocalized forces. The blue curve is the amplitude of the first mechanical resonance, used for probing the photoinduced force with sideband modulation to measure mostly the localized force behavior. The orange curve is the amplitude at the contact resonance frequency, which measures the sample dilation once the tip is in physical contact with the surface. The three curves (blue, green, and red) are normalized by the maximum signal obtained in the sideband excitation. a.u., arbitrary unit.

shifts to contact resonance. At this point, direct-drive PiFM at the contact resonance frequency (shown as the red curve in Fig. 2) essentially measures the thermal expansion of the sample as in photothermal microscopy. The increase in contact resonance PiFM signal with increasing load is likely due to the increase in quality factor of the contact resonance, which generally grows with increasing contact force (*22*).

Experimentally, we can maximize the localized force by modulating the laser intensity at the difference frequency between the cantilever's AFM topographic detection frequency and the PiFM detection frequency ($f_m = f_1 - f_0$), referred to as sideband modulation mode (*23*, *24*). The blue curve in Fig. 2 is the resultant sideband curve, which mostly eliminates the constant nonlocalized force, and is thus sensitive to the localized force alone. The peak position of the PiFM amplitude with sideband modulation occurs farther away from the surface than the direct mode because the sideband signal is affected by the shift in both mechanical resonance frequencies due to the tip-sample force gradient (*23*). The operation in the sideband also prevents the cantilever from sensing the rapid surface dilation that occurs during the arrival of the

laser pulse; instead, the cantilever only senses the time-averaged effect of surface dilation, which is much smaller than the instantaneous dilation. If we assume 1.0 mW of average laser power, the time-averaged surface dilation of PS (one constituent of the BCP) caused by direct absorption of the modulated incident IR radiation is 9.8×10^{-4} Å, which is too small to be recorded by the AFM. The theoretical calculation for this time-averaged sample dilation is provided in the Supplementary Materials.

Point spectra of homopolymers

Sweeping the wavelength of the QCL makes it possible to generate near-field point spectra with PiFM, where the spectral peaks correspond to high PiF responses, indicating increased polarizability. We obtained point PiFM spectra from thin film samples of PS, PMMA, and P2VP [poly(2-vinyl pyridine)] homopolymers as controls for BCP analysis. Figure 3 compares the IR PiFM homopolymer spectra with FTIR spectra generated from thicker films of the same materials in the 1400- to 1800-cm^{-1} spectral range. PiFM spectral acquisition time was 50 ms per wave number step. The PiFM spectra were taken under ambient conditions and are normalized against a spectrum from a Si control sample to remove the effects of QCL power variability. Although the homopolymer films were only nominally 30 nm thick, for each polymer species we observed excellent correlation between the PiFM spectrum and the FTIR spectrum acquired from bulk polymer samples.

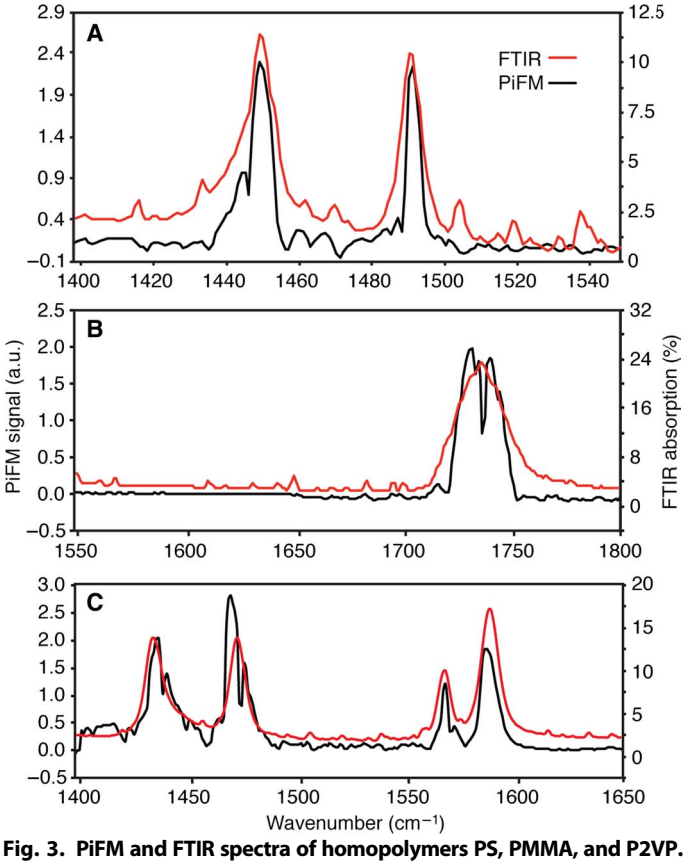

Fig. 3. PiFM and FTIR spectra of homopolymers PS, PMMA, and P2VP. (**A** to **C**) A comparison of PiFM-generated spectra (black lines) and FTIR spectra (red lines) of homopolymers (A) PS, (B) PMMA, and (C) P2VP. The PiFM spectrum is normalized against a Si substrate. The fine structure in the PiFM resonance peaks is due to water absorption in the laser pathway. Each PiFM spectrum was acquired in 1-cm^{-1} steps and dwelling 50 ms for each wave number.

Block copolymers

To demonstrate high spatial resolution combined with chemically specific spectral imaging, we imaged two BCPs using PiFM: PS-*b*-PMMA and PS-*b*-P2VP [poly(styrene-*b*-2-vinyl pyridine)]. BCPs consist of two or more immiscible polymeric segments (blocks) joined by a covalent bond. When thermally annealed or solvent-annealed, they undergo microphase separation, which generates periodic structures of lamellae, cylinders, spheres, or other structures, depending on the volume fraction of each block. The pattern period L_0 depends on the degree of polymerization and the Flory-Huggins interaction parameter χ of the copolymer (*31*). PS-*b*-PMMA is of interest for applications in next-generation lithography for semiconductors (*32*, *33*) and patterned magnetic media (*34*, *35*) because of its ability to easily form periodic lamellae perpendicular to the substrate by a simple thermal annealing process. In the absence of guiding, such lamellae form "fingerprint" structures of periodic wandering lines of alternating PS and PMMA. Highly ordered periodic structures, such as lamellae forming parallel lines over large areas, can be produced by directed self-assembly (DSA) of BCPs with graphoepitaxial (*36*) or chemoepitaxial (*37*) guiding, whereby self-assembled lamellae form patterns commensurate with underlying guiding structures.

Chemical imaging of PS-*b*-PMMA fingerprint patterns

A lamellae-forming PS-*b*-PMMA film with a thickness of approximately 30 nm on a random PS-*r*-PEDCPMA copolymer underlayer yielded a PiFM image of fingerprint lamellae with a natural period (L_0) of 40 nm. The period was verified by Fourier transform analysis of scanning electron microscopy (SEM) images of the fingerprint patterns. To image the PS (or PMMA) component, we tuned the excitation laser to one of its absorption bands at 1492 cm^{-1} (or 1733 cm^{-1}). The scan speed was 0.8 line/s at 256 × 256 pixels for a resulting pixel dwell time of 1.6 ms. The signal integration time is more than three orders of magnitude shorter than a comparable TERS technique (*18*). In Fig. 4, PiFM selectively images the PS and PMMA polymer domains showing the predicted periodicity, including the ability to resolve a small bridge defect, measured to be only ~7 nm wide. The tall contaminant in the topography image is not visible in both PiFM images, indicating that it is a foreign matter. The PiFM response has nonzero values even in regions where unexcited polymer components should be. The nonzero signal comprises the neighboring polymer component due to the tip radius (specified to be less than 50 nm), which is expected to span the pitch of the BCP.

To demonstrate nanoscale point spectroscopy, we generated a 150 × 150–nm (64 × 64 pixels) PiFM image using a wavelength that highlights the PS domains at a scan rate of 0.8 line/s, and then took two point spectra, one each over a lamellar domain of PS and PMMA (see Fig. 4F). Each spectrum was acquired by stepping the wave number by 1 cm^{-1} every 50 ms, for a total of 18 s per spectrum. The spectra are normalized by a PiF spectrum that was acquired on a bare silicon substrate. As expected, when the spectrum is taken with the tip on top of PS (point B and orange curve in Fig. 4F), the two peaks associated with PS at 1452 and 1492 cm^{-1} are clearly observed. Likewise, when the tip is fixed on top of PMMA, the spectrum shows the PMMA peak at 1773 cm^{-1}.

Chemical imaging of PS-*b*-P2VP fingerprint patterns

Imaging of a second lamellar BCP, PS-*b*-P2VP with L_0 = 45 nm, provides a demonstration of PiFM's novel analytical and diagnostic capability on a more complex sample containing separate regions of unguided fingerprint patterns and parallel line patterns formed by DSA. For this

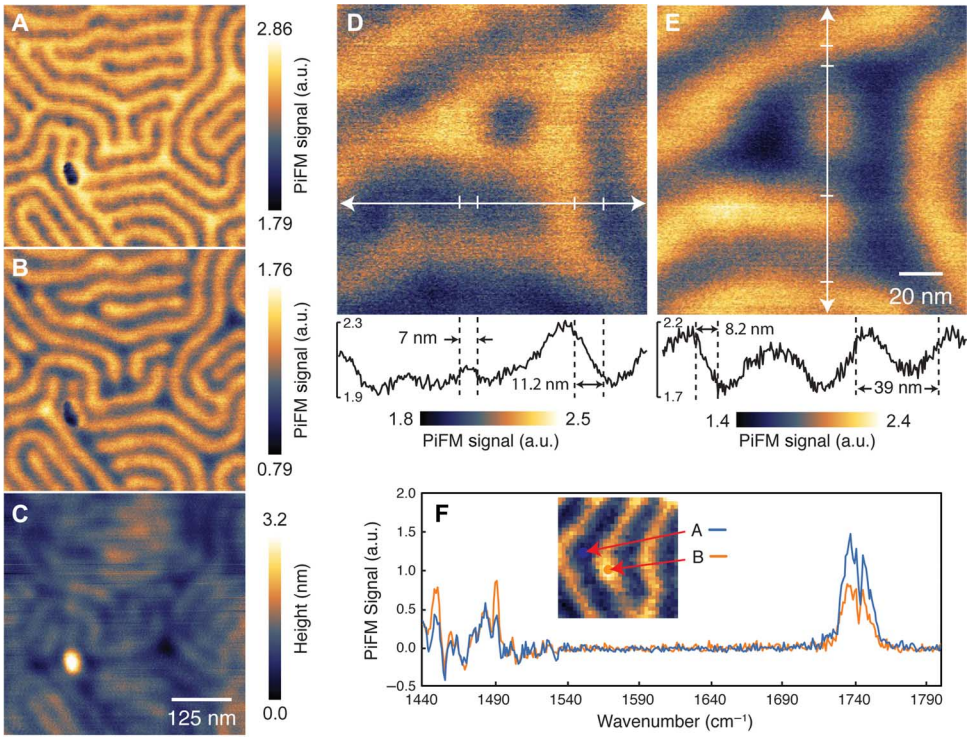

Fig. 4. Chemically selective PiFM imaging of PS-*b*-PMMA. (**A** to **E**) Fingerprint regions of PS-*b*-PMMA observed by PiFM at 1492 cm^{-1} (A and D) and 1733 cm^{-1} (B and E) corresponding to the absorption bands for PS and PMMA, respectively. The topography (C) and PiFM (A or B) signal are obtained simultaneously. (D and E) PiFM resolves the expected ~20-nm-wide domains of the self-assembled BCP with a spatial resolution of <10 nm. (**F**) Normalized point spectra show contributions from the convolution of multiple lamellae due to the tip diameter.

sample, chemical contrast guiding and solvent annealing were used (*38*). It is common practice to selectively stain the P2VP domain to achieve sufficient EM contrast; with PiFM, no additives or modification of the sample is required. The fingerprint region (Fig. 5) was formed over the region of the substrate, consisting solely of an underlayer of PS-*r*-P2VP brush, a neutral surface, which promotes self-assembly of perpendicular lamellae but provides no in-plane guiding. PiFM images were acquired at 0.8 lines/s over a 500 × 500–nm area with 256 × 256 pixels at several different wave numbers: 1447 cm^{-1}, 1452 cm^{-1} (PS), 1469 cm^{-1} (P2VP), 1492 cm^{-1} (PS), and 1589 cm^{-1} (P2VP). These wave numbers were chosen on the basis of point spectra taken at locations over PS and P2VP domains (see Fig. 5E), as well as over an unknown nodule seen in a topographic image of the region. The image in Fig. 5A was taken at 1447 cm^{-1}, which highlighted the unknown nodules. The images in Fig. 5, B and D (based on peaks associated with PS; see Fig. 3A), clearly show PS domains with some subtle differences between them (especially around contaminants). Similarly, the images in Fig. 5, C and E (based on peaks associated with P2VP; see Fig. 3C), show the P2VP domains, clearly demonstrating the complementary placements of P2VP domains with respect to PS domains. Unlike PS, the two peaks associated with P2VP domains do not seem to be significantly affected by the contaminants.

Chemical imaging of PS-*b*-P2VP line patterns created by DSA

Figure 6 shows the DSA region of the PS-*b*-P2VP sample. The guiding patterns under the BCP film in this region consist of periodic straight lines of cross-linked polystyrene (XPS) mat at the 90-nm pitch, with PS-*r*-P2VP brush filling the regions between the XPS lines. During annealing, PS domains of the BCP preferentially align over the XPS lines, whereas the brush areas are nonpreferential. The resulting DSA pattern is an array of the 45-nm pitch (the L_0 of the BCP) alternating PS and P2VP lamellar domains commensurate with the underlying 90-nm pitch guiding pattern, with every other PS line directly over an underlying XPS line. The PiFM images of 500 × 500 nm (256 × 256 pixels) were scanned at 0.8 line/s, using 1492 cm^{-1} to highlight the PS (Fig. 6A) and 1589 cm^{-1} to highlight P2VP (Fig. 6C) domains. The PiFM and topographic images clearly distinguish the domains of the BCP as well as the underlying guiding pattern. The 45-nm pitch of the BCP is prominent in the PiFM images, which highlight the PS and P2VP domains (Fig. 6, A and C). On the other hand, the topographic images (Fig. 6, B and D) show both the 45-nm pitch of the BCP and the 90-nm pitch arising from the XPS guiding lines, with every other line slightly brighter, indicating taller features.

The PiFM image of P2VP (Fig. 6C) shows short sections along the P2VP lines with increased PiF response that correlate with defects in the topography images. This correlation suggests that the defects are additional amounts of P2VP sitting on the top surface. However, the presence of irregular topographic features that are not reflected in either of the PiFM images also hints at the presence of foreign contaminants.

DISCUSSION

The ability of combined PiFM and topographic imaging to show the registration of BCP patterns with underlying guiding patterns provides a

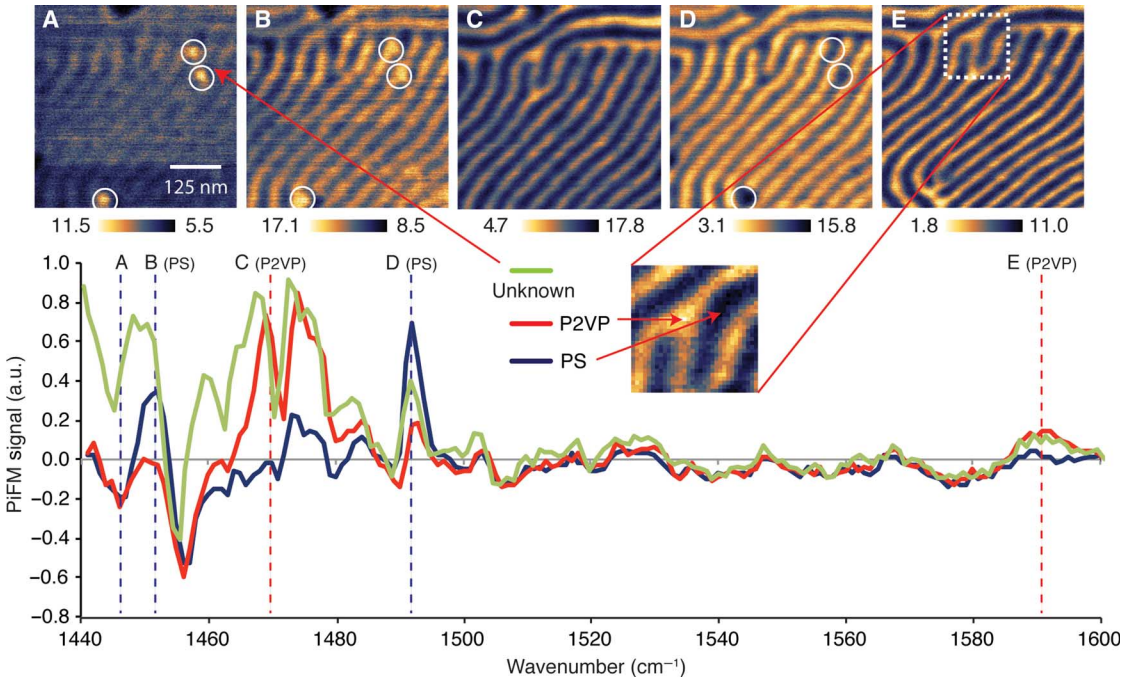

Fig. 5. Fingerprint region of PS-*b*-P2VP. (**A** to **E**) PiFM imaging at (A) 1447 cm^{-1}, (B) 1452 cm^{-1}, (C) 1469 cm^{-1}, (D) 1492 cm^{-1}, and (E) 1589 cm^{-1}. The PiFM point spectra taken from the locations shown in (E) were normalized against a Si background. The different spectral response (green curve) of one of the three nodules clearly visible in (A) suggests that a material other than PS and P2VP may be present.

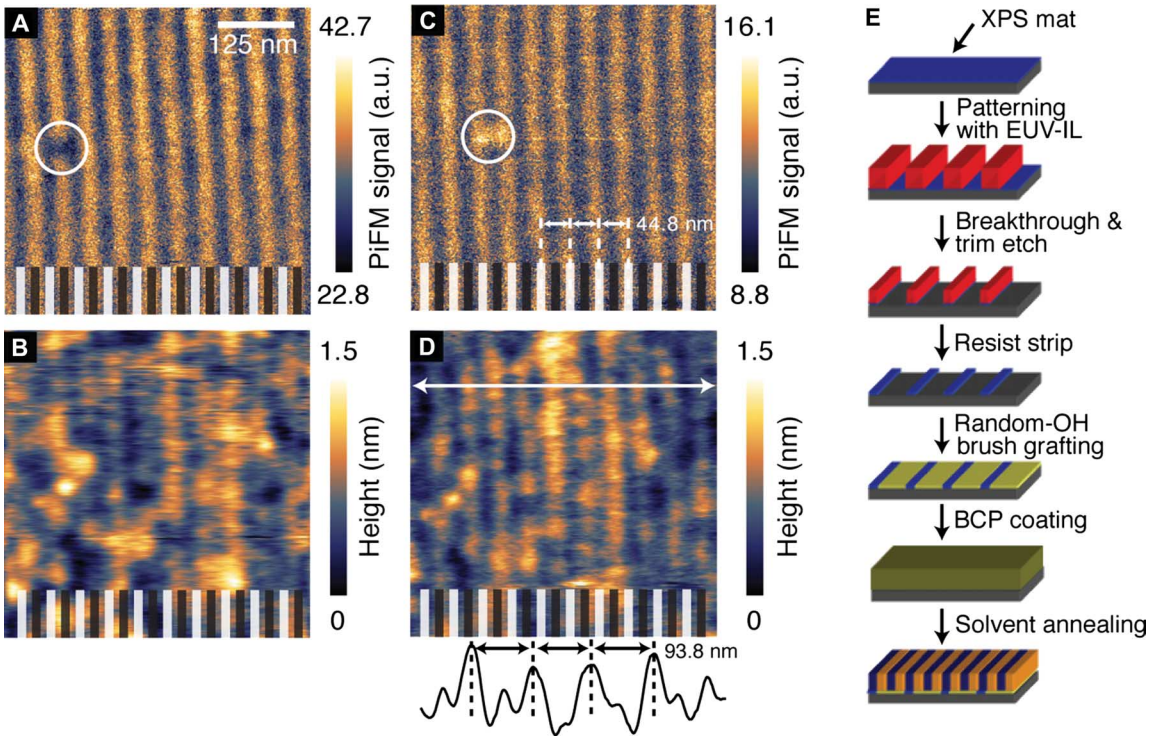

Fig. 6. DSA region of PS-*b*-P2VP. (**A** to **D**) PiFM images at (A) 1492 cm^{-1} and (C) 1589 cm^{-1} selectively image PS and P2VP domains, respectively. Topographic images (B) and (D) were taken simultaneously with images (A) and (C), respectively. Black lines at the bottom of (A) and (B) indicate where PiFM responds to PS lines, whereas white lines at the bottom of (C) and (D) indicate the location of P2VP lines. These colored indicators show that PS domains in the BCP lie directly on the top of topographic ridges, which are attributed to the known topography of XPS lines in the underlying guiding pattern. (**E**) Fabrication steps for the DSA of PS-*b*-P2VP (details are discussed in Materials and Methods). EUV-IL, extreme ultraviolet interference lithography.

useful analytical tool for developing and troubleshooting DSA processes for lithographic applications. PiFM also provides analytical information for contaminants and unexpected structures, providing insight for process improvement and defect reduction.

PiFM will likely find additional applications for BCP materials and process development. As discussed, the capability to image different domain components without infiltration or staining techniques will allow exploration of other potential BCP systems and gain better understanding of domain shape and boundary profiles. PiFM is also expected to help in identifying the existence and chemistry of top-wetting layers in BCPs that exhibit a preferential wetting layer at the film-air interface (*39*). Wetting preferences at both the bottom and top interfaces could also be elucidated by combining the material identification capability of PiFM with the height profiles of topographic AFM in the so-called "island-hole" experiments used to determine wetting properties at both the substrate and top interfaces (*40*, *41*). The potential applications of PiFM in DSA can be extended to the characterization and imaging of the chemical contrast patterns (*38*) (that is, polymer mats and brushes), which are also often difficult to image with conventional EM because these patterns are usually only a few nanometers thin and do not show much height or density contrast.

As noted above, the remarkably high signal-to-noise ratio of PiFM provides for rapid imaging. We were able to image the PS block component (at 1492 cm^{-1}) in our PS-*b*-P2VP sample at line speeds of up to 20 Hz without the loss of spatial resolution. At this scanning rate, an image can be acquired in 6 to 12 s depending on the pixel density, potentially enabling real-time observation of dynamic BCP processes such as pattern coarsening, defect annihilation (*42*, *43*), and progression of thermal or solvent annealing (*44*).

Although the examples discussed here are specific to BCP materials and processes, similar imaging and metrology needs arise in a wide variety of chemically heterogeneous materials systems, with wide technological applications. The rapid advances in nanotechnology require new analytical techniques to characterize both morphology and chemistry of newly synthesized nanomaterials with high sensitivity and spatial resolution. By enabling imaging at the nanometer scale with chemical specificity, nondestructively, and without additives or labeling, PiFM provides a powerful new analytical method for deepening our understanding of nanomaterials and facilitating technological applications of such materials. In movie S1, we demonstrate PiFM hyperspectral imaging, which highlights an advanced ability to find objects of interest, boundary interfaces, and defect analysis via chemical analysis. Work is in progress to demonstrate mid-IR PiFM on other nanostructure systems for materials science and biological applications.

MATERIALS AND METHODS

PS-*r*-PEDCPMA

PS-*r*-PEDCPMA random copolymer was used as a brush layer. PS-*r*-PEDCPMA was synthesized by traditional free-radical polymerization in methyl ethyl ketone, using 2,2′-azobis(2-methylpropionitrile) initiator as described elsewhere (*32*). Using a styrene/epoxydicyclopentadiene methacrylate feed ratio of 75:25, the polymer had a molecular weight of M_n = 4.8 kg/mol and M_w/M_n = 1.50. For casting onto silicon, we prepared a 1 wt % solution of PS-*r*-PEDCPMA combined with an *N*-(trifluoromethylsulfonoxy) phthalimide thermal acid generator (10 wt % relative to polymer) in propylene glycol methyl ether acetate (PGMEA). A silicon substrate was then spin-coated with a 20-nm-thick brush layer that was cross-linked by baking at 220°C for 5 min. After baking, any excess of brush material was removed using a PGMEA rinse step, resulting in a 6-nm-thick layer.

Homopolymers

PS, isotactic PMMA, and P2VP homopolymers were purchased from Polymer Source Inc. and used as received. The PS homopolymer has a molecular weight of M_n = 22.5 kg/mol and M_w/M_n = 1.06. The PMMA homopolymer has a molecular weight of M_n = 15.6 kg/mol and M_w/M_n = 1.09, and P2VP homopolymer has a molecular weight of M_n = 97 kg/mol and M_w/M_n = 1.08. All homopolymers were spin-coated onto silicon substrates from a 1 wt % solution in PGMEA, resulting in a film thickness of 27 nm (PS), 27 nm (PVP), and 30 nm (PMMA).

PS-*b*-PMMA

The lamellae-forming BCP PS-*b*-PMMA used in this study was purchased from Polymer Source Inc. and used as received. The molecular weight and composition, as measured by size-exclusion chromatography and ^{1}H-NMR (nuclear magnetic resonance) spectroscopy, is M_n(PS) = 33 kg/mol and M_n(PMMA) = 33 kg/mol with M_w/M_n = 1.09. For the orientation control of the lamellae, with respect to the substrate, we used the same procedure for the PS-*r*-PEDCPMA brush method, as described above. After preparation of the underlayer, a film of PS-*b*-PMMA was deposited onto the sample by spin-coating of a 1 wt % solution in PGMEA and subsequent thermal annealing at 200°C for 5 min. After thermal annealing, the BCP film thickness was approximately 30 nm.

PS-*b*-P2VP

The first step involved the creation of chemical contrast guiding patterns following the Liu-Nealey (LiNe) process (*38*), illustrated in Fig. 6E. A silicon substrate was coated with an XPS mat, with an approximate thickness of 7 nm. The XPS mat was, in turn, coated with PMMA photoresist and patterned using an extreme ultraviolet interference lithography system at the University of Wisconsin to create guiding line patterns at the 90-nm pitch (approximately twice the expected BCP pattern pitch) in rectangular areas. The PMMA pattern was transferred to the XPS mat via O_2 reactive ion etch, with etching parameters adjusted to overetch the line pattern to create a low duty cycle (less than 50% XPS line; more than 50% exposed substrate surface). The remaining PMMA was stripped, leaving the XPS line patterns. The exposed substrate surface was then backfilled with random PS-*r*-P2VP brush (containing 50% styrene and hydroxyl functional groups) with a thickness of approximately 3 to 5 nm. The resulting pattern of XPS lines with a PS-*r*-P2VP brush background served as the chemical contrast-guiding pattern for subsequent DSA of PS-*b*-P2VP. After the preparation of the guiding patterns, a film of PS-*b*-P2VP (M_n = 40.5-*b*-40.0 kg/mol) BCP dissolved in dimethylfuran was deposited on the sample by spin coating. After solvent evaporation, the BCP film thickness was approximately 30 nm. The sample was solvent-annealed for a few hours in acetone vapor in a closed container at room temperature. Phase separation and formation of lamellar patterns occurred during the annealing process; these patterns remained stable after removal from the annealing container and evaporation of solvent from the sample.

The PS-*b*-P2VP sample used in this study had been prepared for a different purpose several years before this work. At the time of its preparation, it was stained by exposure to iodine vapor, which enabled SEM imaging (iodine is absorbed preferentially into the P2VP phase of the BCP, providing some minimal contrast for imaging). However,

iodine staining is not stable over a period of years, so the iodine is expected to have evaporated, leaving the sample with no significant amount of iodine at the time of the experiments reported here. The SEM studies performed at the time of sample preparation confirmed the formation of the expected lamellar patterns, and cross-sectional SEM images indicated that no wetting layer was present on the top surface of the BCP film; vertical lamellae extend to the top surface.

FTIR spectra

The bulk IR measurements were done using a Thermo Nicolet NEXUS 670 FTIR instrument with a resolution of 2 cm^{-1}, a spectral range from 350 to 4000 cm^{-1}, and 64 scans for each sample. The spectral resolution of the spectrometer is 0.125 cm^{-1}, and it is continuously purged with dry, CO_2-free air. We used a deuterated triglycine sulfate with KBr detector and a KBr beam splitter. Before the measurements, thick films (500 nm) of the homopolymers were prepared on thin silicon wafers and measured in transmission. A blank wafer was used for background measurement.

PiFM measurements

A VistaScope microscope from Molecular Vista Inc. was coupled to a LaserTune QCL product with a wave number resolution of 0.5 cm^{-1} and a tuning range from 800 to 1800 cm^{-1} from Block Engineering. The microscope was operated in dynamic mode, with NCH-Au 300 kHz noncontact cantilevers from Nanosensors.

Contact resonance measurement

The microscope was operated in contact mode, the DC component of the measurement was used for topographical tracking, and the AC component of the resonance was monitored by a lock-in at the contact resonance. Using PPP-FMAu 60-kHz cantilevers, we determined the contact resonance to be 262 kHz for the particular cantilever used during the experiment.

SUPPLEMENTARY MATERIALS

Supplementary material for this article is available at http://advances.sciencemag.org/cgi/content/full/2/3/e1501571/DC1

Text

Fig. S1. Schematic for thermal calculation: A gold-coated probe with end radius *a* in the vicinity of PS on a silicon substrate.

Movie S1. Demonstration of hyperspectral photoinduced force imaging on a BCP composed of P2VP and PS.

References (*45*, *46*)

REFERENCES AND NOTES

1. C. T. Black, R. Ruiz, G. Breyta, J. Y. Cheng, M. E. Colburn, K. W. Guarini, H.-C. Kim, Y. Zhang, Polymer self assembly in semiconductor microelectronics. *IBM J. Res. Dev.* **51**, 605–633 (2007).
2. P. R. Delgadillo, M. Suri, S. Durant, A. Cross, V. R. Nagaswami, D. Van Den Heuvel, R. Gronheid, P. Nealey, Defect source analysis of directed self-assembly process. *J. Micro. Nanolithogr. MEMS MOEMS* **12**, 031112 (2013).
3. F. I. Allen, M. Watanabe, Z. Lee, N. P. Balsara, A. M. Minor, Chemical mapping of a block copolymer electrolyte by low-loss EFTEM spectrum-imaging and principal component analysis. *Ultramicroscopy* **111**, 239–244 (2011).
4. M. Park, C. Harrison, P. M. Chaikin, R. A. Register, D. H. Adamson, Block copolymer lithography: Periodic arrays of ~10^{11} holes in 1 square centimeter. *Science* **276**, 1401–1404 (1997).
5. J. Chai, D. Wang, X. Fan, J. M. Buriak, Assembly of aligned linear metallic patterns on silicon. *Nat. Nanotechnol.* **2**, 500–506 (2007).
6. Q. Peng, Y.-C. Tseng, S. B. Darling, J. W. Elam, Nanoscopic patterned materials with tunable dimensions via atomic layer deposition on block copolymers. *Adv. Mater.* **22**, 5129–5133 (2010).
7. R. Ruiz, L. Wan, J. Lille, K. C. Patel, E. Dobisz, D. E. Johnston, K. Kisslinger, C. T. Black, Image quality and pattern transfer in directed self assembly with block-selective atomic layer deposition. *J. Vac. Sci. Technol. B* **30**, 06F202 (2012).
8. D. W. Pohl, W. Denk, M. Lanz, Optical stethoscopy: Image recording with resolution λ/20. *Appl. Phys. Lett.* **44**, 651–653 (1984).
9. E. Betzig, J. K. Trautman, T. D. Harris, J. S. Weiner, R. L. Kostelak, Breaking the diffraction barrier: Optical microscopy on a nanometric scale. *Science* **251**, 1468–1470 (1991).
10. F. Zenhausern, Y. Martin, H. K. Wickramasinghe, Scanning interferometric apertureless microscopy: Optical imaging at 10 angstrom resolution. *Science* **269**, 1083–1085 (1995).
11. R. M. Stöckle, Y. D. Suh, V. Deckert, R. Zenobi, Nanoscale chemical analysis by tip-enhanced Raman spectroscopy. *Chem. Phys. Lett.* **318**, 131–136 (2000).
12. A. Hartschuh, E. J. Sánchez, X. S. Xie, L. Novotny, High-resolution near-field Raman microscopy of single-walled carbon nanotubes. *Phys. Rev. Lett.* **90**, 095503 (2003).
13. E. A. Pozzi, M. D. Sonntag, N. Jiang, J. M. Klingsporn, M. C. Hersam, R. P. Van Duyne, Tip-enhanced Raman imaging: An emergent tool for probing biology at the nanoscale. *ACS Nano* **7**, 885–888 (2013).
14. B. Knoll, F. Keilmann, Near-field probing of vibrational absorption for chemical microscopy. *Nature* **399**, 134–137 (1999).
15. N. Ocelic, A. Huber, R. Hillenbrand, Pseudoheterodyne detection for background-free near-field spectroscopy. *Appl. Phys. Lett.* **89**, 101124 (2006).
16. B. Pollard, E. A. Muller, K. Hinrichs, M. B. Raschke, Vibrational nano-spectroscopic imaging correlating structure with intermolecular coupling and dynamics. *Nat. Commun.* **5**, 3587 (2014).
17. T. Schmid, L. Opilik, C. Blum, R. Zenobi, Nanoscale chemical imaging using tip-enhanced Raman spectroscopy: A critical review. *Angew. Chem. Int. Ed.* **52**, 5940–5954 (2013).
18. L. Xue, W. Li, G. G. Hoffmann, J. G. P. Goossens, J. Loos, G. de With, High-resolution chemical identification of polymer blend thin films using tip-enhanced Raman mapping. *Macromolecules* **44**, 2852–2858 (2011).
19. A. Dazzi, R. Prazeres, F. Glotin, J. M. Ortega, Local infrared microspectroscopy with subwavelength spatial resolution with an atomic force microscope tip used as a photothermal sensor. *Opt. Lett.* **30**, 2388–2390 (2005).
20. B. Lahiri, G. Holland, A. Centrone, Chemical imaging beyond the diffraction limit: Experimental validation of the PTIR technique. *Small* **9**, 439–445 (2013).
21. F. Lu, M. Jin, M. A. Belkin, Tip-enhanced infrared nanospectroscopy via molecular expansion force detection. *Nat. Photonics* **8**, 307–312 (2014).
22. A. Caron, W. Arnold, Observation of local internal friction and plasticity onset in nanocrystalline nickel by atomic force acoustic microscopy. *Acta Mater.* **57**, 4353–4363 (2009).
23. I. Rajapaksa, K. Uenal, H. K. Wickramasinghe, Image force microscopy of molecular resonance: A microscope principle. *Appl. Phys. Lett.* **97**, 073121 (2010).
24. I. Rajapaksa, H. K. Wickramasinghe, Raman spectroscopy and microscopy based on mechanical force detection. *Appl. Phys. Lett.* **99**, 161103 (2011).
25. J. Jahng, J. Brocious, D. A. Fishman, F. Huang, X. Li, V. A. Tamma, H. K. Wickramasinghe, E. O. Potma, Gradient and scattering forces in photoinduced force microscopy. *Phys. Rev. B.* **90**, 155417 (2014).
26. J. Jahng, J. Brocious, D. A. Fishman, S. Yampolsky, D. Nowak, F. Huang, V. A. Apkarian, H. K. Wickramasinghe, E. O. Potma, Ultrafast pump-probe force microscopy with nanoscale resolution. *Appl. Phys. Lett.* **106**, 083113 (2015).
27. K. Dholakia, P. Zemánek, *Colloquium*: Gripped by light: Optical binding. *Rev. Mod. Phys.* **82**, 1767–1791 (2010).
28. J. R. Arias-González, M. Nieto-Vesperinas, Optical forces on small particles: Attractive and repulsive nature and plasmon-resonance conditions. *J. Opt. Soc. Am. A* **20**, 1201–1209 (2003).
29. L. Novotny, B. Hecht, *Principles of Nano-Optics* (Cambridge Univ. Press, Cambridge, 2012).
30. F. Huang, V. A. Tamma, Z. Mardy, J. Burdett, H. K. Wickramasinghe, Imaging nanoscale electromagnetic near-field distributions using optical forces. *Sci. Rep.* **5**, 10610 (2015).
31. F. S. Bates, G. H. Fredrickson, Block copolymer thermodynamics: Theory and experiment. *Annu. Rev. Phys. Chem.* **41**, 525–557 (1990).
32. G. S. Doerk, J. Y. Cheng, G. Singh, C. T. Rettner, J. W. Pitera, S. Balakrishnan, N. Arellano, D. P. Sanders, Enabling complex nanoscale pattern customization using directed self-assembly. *Nat. Commun.* **5**, 5805 (2014).
33. H. Tsai, J. W. Pitera, H. Miyazoe, S. Bangsaruntip, S. U. Engelmann, C.-C. Liu, J. Y. Cheng, J. J. Bucchignano, D. P. Klaus, E. A. Joseph, D. P. Sanders, M. E. Colburn, M. A. Guillorn, Two-dimensional pattern formation using graphoepitaxy of PS-*b*-PMMA block copolymers for advanced FinFET device and circuit fabrication. *ACS Nano* **8**, 5227–5232 (2014).
34. T. R. Albrecht, H. Arora, V. Ayanoor-Vitikkate, J.-M. Beaujour, D. Bedau, D. Berman, A. L. Bogdanov, Y.-A. Chapuis, J. Cushen, E. E. Dobisz, G. Doerk, H. Gao, M. Grobis, B. Gurney, W. Hanson, O. Hellwig, T. Hirano, P.-O. Jubert, D. Kercher, J. Lille, Z. Liu, C. M. Mate, Y. Obukhov, K. C. Patel, K. Rubin, R. Ruiz, M. Schabes, L. Wan, D. Weller, T.-W. Wu, E. Yang, Bit-patterned magnetic recording: Theory, media fabrication, and recording performance. *IEEE Trans. Magn.* **51**, 1–42 (2015).
35. R. Ruiz, H. Kang, F. A. Detcheverry, E. Dobisz, D. S. Kercher, T. R. Albrecht, J. J. de Pablo, P. F. Nealey, Density multiplication and improved lithography by directed block copolymer assembly. *Science* **321**, 936–939 (2008).

36. S.-M. Park, M. P. Stoykovich, R. Ruiz, Y. Zhang, C. T. Black, P. F. Nealey, Directed assembly of lamellae-forming block copolymers by using chemically and topographically patterned substrates. *Adv. Mater.* **19**, 607–611 (2007).
37. S. O. Kim, H. H. Solak, M. P. Stoykovich, N. J. Ferrier, J. J. de Pablo, P. F. Nealey, Epitaxial self-assembly of block copolymers on lithographically defined nanopatterned substrates. *Nature* **424**, 411–414 (2003).
38. C.-C. Liu, E. Han, M. S. Onses, C. J. Thode, S. Ji, P. Gopalan, P. F. Nealey, Fabrication of lithographically defined chemically patterned polymer brushes and mats. *Macromolecules* **44**, 1876–1885 (2011).
39. C. Harrison, M. Park, P. Chaikin, R. A. Register, D. H. Adamson, N. Yao, Depth profiling block copolymer microdomains. *Macromolecules* **31**, 2185–2189 (1998).
40. R. D. Peters, X. M. Yang, T. K. Kim, P. F. Nealey, Wetting behavior of block copolymers on self-assembled films of alkylchlorosiloxanes: Effect of grafting density. *Langmuir* **16**, 9620–9626 (2000).
41. R. D. Peters, X. M. Yang, P. F. Nealey, Morphology of thin films of diblock copolymers on surfaces micropatterned with regions of different interfacial energy. *Macromolecules* **35**, 1822–1834 (2002).
42. R. Ruiz, J. K. Bosworth, C. T. Black, Effect of structural anisotropy on the coarsening kinetics of diblock copolymer striped patterns. *Phys. Rev. B* **77**, 054204 (2008).
43. L. Tsarkova, A. Knoll, R. Magerle, Rapid transitions between defect configurations in a block copolymer melt. *Nano Lett.* **6**, 1574–1577 (2006).
44. M. Y. Paik, J. K. Bosworth, D.-M. Smilges, E. L. Schwartz, X. Andre, C. K. Ober, Reversible morphology control in block copolymer films via solvent vapor processing: An in situ GISAXS study. *Macromolecules* **43**, 4253–4260 (2010).
45. Y. C. Martin, H. F. Hamann, H. K. Wickramasinghe, Strength of the electric field in apertureless near-field optical microscopy. *J. Appl. Phys.* **89**, 5774–5778 (2001).
46. A. C. Tam, Applications of photoacoustic sensing techniques. *Rev. Mod. Phys.* **58**, 381–431 (1986).

Acknowledgments: We acknowledge P. Nealey and the University of Wisconsin for the use of facilities and resources in the preparation of the PS-*b*-P2VP sample and Block Engineering for the loan of their LaserTune QCL. We thank T. P. Magbitang from IBM Research for taking FTIR measurements on the homopolymer samples and G. Singh for the preparation of the PS-*b*-PMMA sample. **Funding:** This research was partially supported by the NSF's Small Business Innovation Research award no. 1353524. **Author contributions:** D.N., HK.W., T.R.A., and S.P. designed the experiment. J.J. provided the theoretical analysis supervised by E.P. Homopolymer samples and background information about the PS-*b*-PMMA and FTIR measurements were prepared by K.S. and supervised by D.P.S. and J.F. The PS-*b*-P2VP samples were prepared by L.W. and R.R. The experiment was conducted by W.M., with guidance from D.N. and S.P. The paper was written by D.N., T.R.A., S.P., R.R., and K.S. The supplemental note and calculation were provided by H.K.W. All authors discussed the experimental results. **Competing interests:** The authors declare that they have no competing interests. **Data and materials availability:** All data needed to evaluate the conclusions in the paper are present in the paper and/or the Supplementary Materials. Additional data related to this paper may be requested from the authors.

Submitted 4 November 2015
Accepted 14 January 2016
Published 25 March 2016
10.1126/sciadv.1501571

Citation: D. Nowak, W. Morrison, H. K. Wickramasinghe, J. Jahng, E. Potma, L. Wan, R. Ruiz, T. R. Albrecht, K. Schmidt, J. Frommer, D. P. Sanders, S. Park, Nanoscale chemical imaging by photoinduced force microscopy. *Sci. Adv.* **2**, e1501571 (2016).

ScienceAdvances
AAAS

Nanoscale chemical imaging by photoinduced force microscopy

Derek Nowak, William Morrison, H. Kumar Wickramasinghe, Junghoon Jahng, Eric Potma, Lei Wan, Ricardo Ruiz, Thomas R. Albrecht, Kristin Schmidt, Jane Frommer, Daniel P. Sanders and Sung Park (March 25, 2016)

Sci Adv 2016, 2:.
doi: 10.1126/sciadv.1501571